Anomalous perovskite $PbRuO_3$ stabilized under high pressure

J.-G. Cheng[a,b,1], K. E. Kweon[c,1], J.-S. Zhou[a,2], J. A. Alonso[d], P.-P. Kong[b], Y. Liu[b], Changqing Jin[b], Junjie Wu[b,e], Jung-Fu Lin[e], S. A. Larregola[a], Wenge Yang[f], Guoyin Shen[f], A. H. MacDonald[g], Arumugam Manthiram[a], G. S. Hwang[c,2], and John B. Goodenough[a,2]

[a]Materials Science and Engineering Program and Texas Materials Institute, The University of Texas at Austin, Austin, TX 78712; [b]Institute of Physics, Chinese Academy of Sciences, Beijing 100190, China; [c]Chemical Engineering and Texas Materials Institute, The University of Texas at Austin, Austin, TX 78712; [d]Department of Energy, Instituto de Ciencia de Materiales de Madrid, Consejo Superior de Cientificas, 28049 Madrid, Spain; [e]Department of Geological Sciences, Jackson School of Geosciences, The University of Texas at Austin, Austin, TX 78712; [f]High Pressure Synergetic Consortium and High Pressure Collaborative Access Team, Geophysical Laboratory, Carnegie Institution of Washington, Argonne, IL 60439; and [g]Department of Physics and Texas Materials Institute, The University of Texas at Austin, Austin, TX 78712

Contributed by John B. Goodenough, October 22, 2013 (sent for review May 22, 2013)

Perovskite oxides ABO_3 are important materials used as components in electronic devices. The highly compact crystal structure consists of a framework of corner-shared BO_6 octahedra enclosing the A-site cations. Because of these structural features, forming a strong bond between A and B cations is highly unlikely and has not been reported in the literature. Here we report a pressure-induced first-order transition in $PbRuO_3$ from a common orthorhombic phase (*Pbnm*) to an orthorhombic phase ($Pbn2_1$) at 32 GPa by using synchrotron X-ray diffraction. This transition has been further verified with resistivity measurements and Raman spectra under high pressure. In contrast to most well-studied perovskites under high pressure, the $Pbn2_1$ phase of $PbRuO_3$ stabilized at high pressure is a polar perovskite. More interestingly, the $Pbn2_1$ phase has the most distorted octahedra and a shortest Pb—Ru bond length relative to the average Pb—Ru bond length that has ever been reported in a perovskite structure. We have also simulated the behavior of the $PbRuO_3$ perovskite under high pressure by first principles calculations. The calculated critical pressure for the phase transition and evolution of lattice parameters under pressure match the experimental results quantitatively. Our calculations also reveal that the hybridization between a Ru:t_{2g} orbital and an sp hybrid on Pb increases dramatically in the *Pbnm* phase under pressure. This pressure-induced change destabilizes the *Pbnm* phase to give a phase transition to the $Pbn2_1$ phase where electrons in the overlapping orbitals form bonding and antibonding states along the shortest Ru—Pb direction at $P > P_c$.

$PbRuO_3$ crystallizes in the orthorhombic perovskite structure with the *Pbnm* space group; it is metallic and exhibits no long-range magnetic ordering down to the lowest temperature. Compared with other Pb-based ferroelectric perovskites like $PbTiO_3$ (1–4), the orthorhombic *Pbnm* $PbRuO_3$ has not been extensively studied in part because it needs to be synthesized at high temperature and under high pressure. $PbRuO_3$ has gained attention in recent years after the report of a phase transition to a new orthorhombic *Imma* phase on cooling through a $T_t \sim 90$ K (5, 6). An increased octahedral-site distortion in the phase at $T < T_t$ led Kimber et al. (5) to speculate orbital ordering of the 4*d* electrons at Ru^{4+}. The bond-length mismatch due to the tolerance factor $t \equiv (A—O)/\sqrt{2}(B—O) < 1$, where (A—O) and (B—O) are average equilibrium bond lengths, can be relieved by cooperative octahedral-site rotations that give rise to rich tilting systems in the perovskite structure (7–9). Because the thermal expansion coefficient of the A—O bond is normally larger than that of the B—O bond in an ABO_3 perovskite, *t* increases with increasing temperature, which results in a series of structures with progressively increasing symmetry in the order of *Pbnm* → *Imma* (*P4/mbm*, *I4/mcm*, *R-3c*) → *Pm-3m* (10, 11). The unusual phase transition to a structure with higher symmetry at low temperatures found in $PbRuO_3$ motivated us to carry out a structural study under high pressure.

Results and Discussion

Generally speaking, the pressure effect on a *Pbnm* perovskite with *t* less than but close to 1 is similar to the effect with increasing temperature (11); phase transitions in the order of *Pbnm* → *Imma* (*P4/mbm*, *I4/mcm*, *R-3c*) → *Pm-3m* are expected with increasing pressure. The high-pressure structural study with synchrotron X-ray diffraction (SXRD) in a diamond anvil cell (DAC) (see the *Supporting Information* for the detail of sample's preparation and measurements) reveals that at room temperature the *Pbnm* phase remains stable up to 32 GPa followed by a phase transition with further increase of pressure (Fig. 1*A*). However, an increased number of diffraction peaks suggested that the high-pressure phase may have an even lower symmetry. We have also confirmed the pressure-induced phase transition with Raman spectroscopy under high pressure (Fig. 1*B*). The spectra were decomposed by fitting them with Lorentzian components. Almost all major Raman active modes (bands A–H) associated with the *Pbnm* structure change gradually with pressure to 37 GPa. At least five new Raman active modes (bands I–V) appear abruptly for $P > 32$ GPa (Fig. 1*C*). Consistent with the high-pressure SXRD study, an increased number of Raman active modes in the phase at $P > 32$ GPa indicates that the high-pressure phase has a lower symmetry. However, it is impossible to resolve the crystal structure by Raman spectra alone.

Significance

Perovskites had the highest density in oxides and fluorides with the formula ABX_3 before the postperovskite structure was found in $MgSiO_3$ under high temperature and high pressure. The densification of a perovskite under pressure can be realized by shortening A—X and B—X bond lengths and cooperative rotations of octahedra. In most cases, the densification is within the same space group. The behavior of $PbRuO_3$ under high pressure offers a case where the perovskite structure can be densified by significantly shortening the A–B distance and distorting the octahedra. Forming such a highly unusual structure by Pb—Ru bonding shows the flexibility of the perovskite structure to avoid collapsing into the postperovskite structure.

Author contributions: J.-G.C. and J.-S.Z. designed research; J.-G.C., K.E.K., J.-S.Z., P.-P.K., Y.L., C.J., and G.S.H. performed experiments; J.-G.C., K.E.K., J.-S.Z., J.A.A., S.A.L., A.H.M., G.S.H., and J.B.G. analyzed data; J.W., J.-F.L., W.Y., G.S., and A.M. contributed new reagents/analytic tools; and J.-G.C., K.E.K., J.-S.Z., G.S.H., and J.B.G. wrote the paper.

The authors declare no conflict of interest.

[1]J.-G.C. and K.E.K. contributed equally to this work.

[2]To whom correspondence may be addressed. E-mail: jgoodenough@mail.utexas.edu, jszhou@mail.utexas.edu, or gshwang@che.utexas.edu.

This article contains supporting information online at www.pnas.org/lookup/suppl/doi:10.1073/pnas.1318494110/-/DCSupplemental.

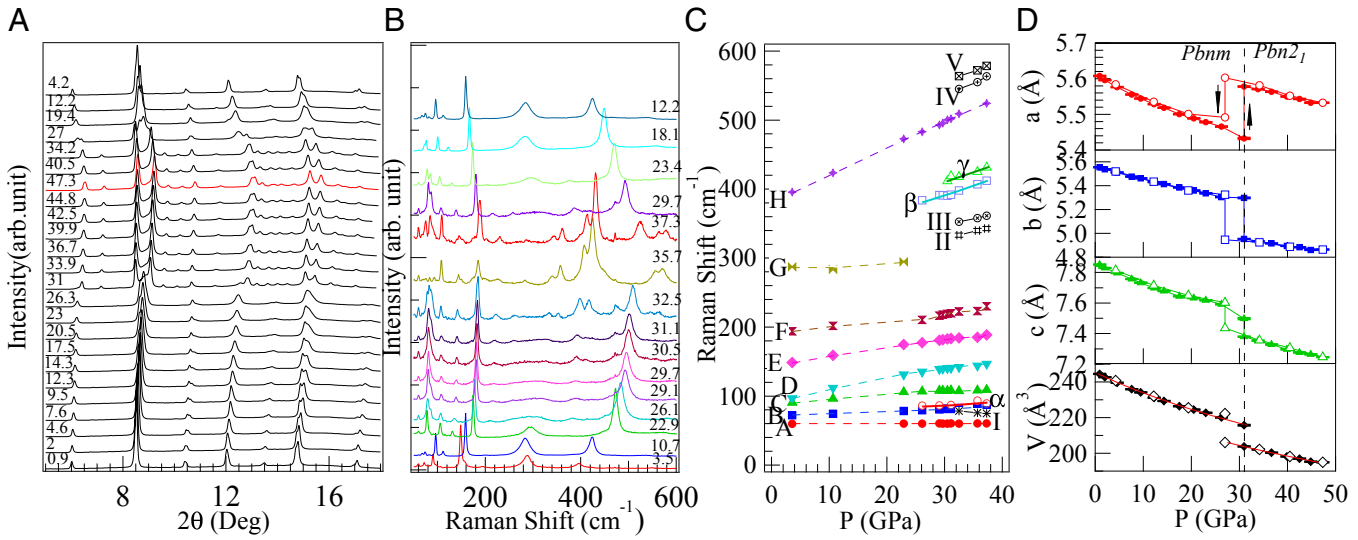

Fig. 1. (*A*) Evolution of the SXRD patterns of the $PbRuO_3$ perovskite as a function of pressure at room temperature. Values are pressure in gigapascals. (*B*) Raman spectra under different pressures. (*C*) The pressure dependence of Raman active modes. (*D*) Pressure dependence of the lattice parameters; arrows inside the plot point to the direction of increasing pressure. The solid lines are the Birch–Murnaghan fitting curves to the experimental *V*(*P*) data.

Initial trials with either the *C1c1* (No. 9) or the $Pbn2_1$ (No. 33) structural model gave a reasonable fit to the SXRD pattern of the phase at $P > P_c$, see Figs. S1 and S2 and Tables S1 and S2 for details of the structural refinement. The two structural models differ only in the oxygen positions about which the SXRD provides very limited information. Our density functional theory (DFT) calculation has shown that the $Pbn2_1$ structure has a lower ground-state energy than that of the *Pbnm* structure at high pressure. The input of optimized oxygen positions from the DFT calculations improves further the structural refinement. The structural refinement and the DFT calculation are complementary tools for resolving the crystal structure in our study. Although the mirror symmetry plane in the *Pbnm* structure is missing in the polar $Pbn2_1$ structure, some $GdFeO_3$-type perovskites can be refined reasonably well with both the *Pbnm* and $Pbn2_1$ structural models (12). The perovskite $BiInO_3$ is the only case so far where fitting with a polar structural model $Pbn2_1$ is clearly better than that with the nonpolar *Pbnm* structure (13). The polar structure of $BiInO_3$ becomes unstable against the *Pbnm* structure at $P \sim 1.5$ GPa and a first-order change with 2% volume drop on crossing the $Pbn2_1$ to the *Pbnm* structural transition has been observed (14), which matches the popular scenario that high pressure prefers a higher symmetry structure in a perovskite structure with $t < 1$ but close to 1. In the case of perovskite $PbRuO_3$, however, the polar structure is stabilized under high pressure and the difference of SXRD patterns between the *Pbnm* and $Pbn2_1$ phases in Fig. 1*A* is even more remarkable than in the case of $BiInO_3$.

The pressure dependences of the unit-cell parameters of $PbRuO_3$ in Fig. 1*D* show a general contraction of *a, b, c,* and V within the *Pbnm* phase with increasing pressure; but at $P_c \sim 32$ GPa, *a* jumps and all other lattice parameters *b, c,* and V drop abruptly with as large as 6% volume change on crossing the phase transition. An abrupt change of the cell volume and the pressure hysteresis at P_c indicate a first-order transition. The pressure dependence of the volume for both phases has been fitted with the Birch–Murnaghan (BM) equation of solid lines in Fig. 1*D* (see the *Supporting Information* for the detail of BM equation). By using fixed $B' = 4$ in the BM equation, we obtained a bulk modulus $B_0 = 189.8(3)$ GPa for the *Pbnm* phase and $B_0 = 205(1)$ GPa for the $Pbn2_1$ phase, respectively.

For a perovskite structure with tilting systems, regular octahedra are not compatible with fixed rotations axes (15). As

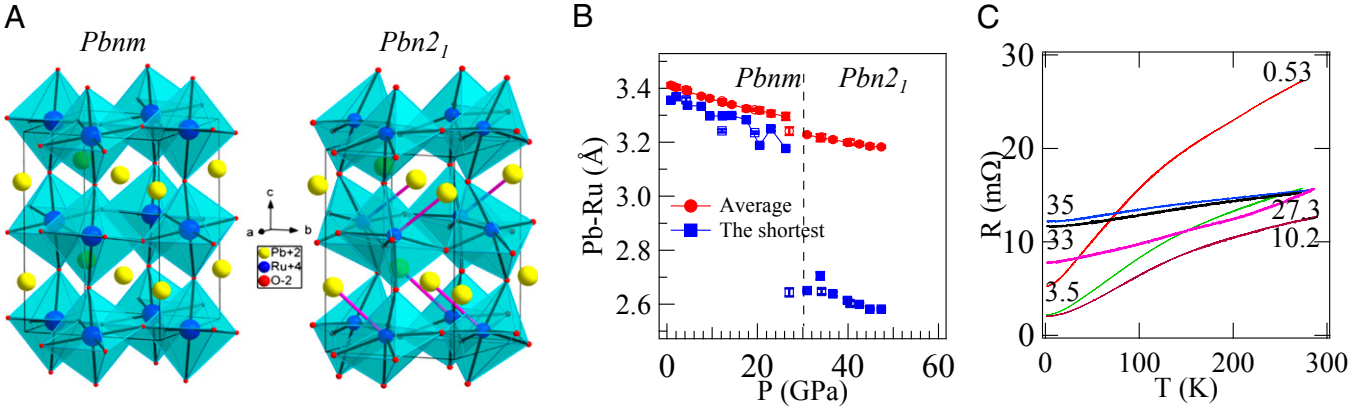

Fig. 2. (*A*) Two perovskite structures of $PbRuO_3$. (*B*) Pressure dependence of the average and shortest Pb—Ru distances of the $PbRuO_3$ perovskite. (*C*) The temperature dependence of resistance under different pressures.

a typical site distortion, the O_{21}—M—O_{22} bond angle α opening to the *b* axis becomes less than 90° as $t \to 1$ (16). Development of this angular site distortion changes the relationship between lattice parameters from $a < c/\sqrt{2} \leq b$ to $a > b \sim c/\sqrt{2}$. $PbRuO_3$ shows $a > b \sim c/\sqrt{2}$ at ambient pressure, which indicates an α < 90°. A further increase of *a*-*b* in $PbRuO_3$ under pressure of Fig. S3 is typical for a *Pbnm* perovskite like $LaGaO_3$ (17, 18), $LaCrO_3$ (19, 20), and $SmNiO_3$ (21). An increased angular site distortion makes these *Pbnm* perovskites unstable against the higher symmetry *R3-c* phase under high pressure. Pressure appears to play the same role in the *Pbnm* phase of $PbRuO_3$ as in other *Pbnm* perovskites in terms of lattice-parameter changes and, therefore, the site distortion; but this regular pressure dependence of lattice parameters in the *Pbnm* phase of $PbRuO_3$ ends up with an irregular phase transition to a polar perovskite with even lower symmetry at $P > P_c$.

In the *Pbnm* phase of $PbRuO_3$, Fig. 2*A*, the Pb ions are located in the void formed by the eight corner–shared $RuO_{6/2}$ octahedra, resulting in an average Pb—Ru distance of about $(\sqrt{3}/2)a_p \sim$ 3.46 Å, where $a_p \sim (a, b, c/\sqrt{2})/\sqrt{2}$ is the primary cell parameter. In the plot of the Pb—Ru distance in Fig. 2*B*, the average value the Pb—Ru distance decreases gradually from 3.4 to 3.2 Å with increasing pressure from 0 to 47.3 GPa and there is only a very small drop of the averaged value on crossing the transition to the *Pbn2₁* phase. The cooperative rotation of the $RuO_{6/2}$ octahedra in the *Pbnm* phase makes the Pb atoms shift slightly away from the center, resulting in four Pb—Ru distances about 0.05 Å shorter than the average value. In comparison, cooperative rotations of highly distorted octahedra in the *Pbn2₁* phase of Fig. 2*A* create eight different Pb—Ru distances. Most strikingly, a single Pb—Ru distance reaches as small as 2.6 Å in the *Pbn2₁* phase, which is about 0.6 Å shorter than the average value, which is unprecedented in all known perovskite oxides. The octahedra in the *Pbn2₁* phase are highly distorted as is shown in Fig. 2*A*; the four O^{2-} ions of an RuO_2 basal plane are not within a plane and the apical oxygen, especially the top one, deviates severely from the axis coming through the center normal to the RuO_2 basal plane of an octahedron to yield a space for the shortest Pb—Ru distance. The average Ru—O—Ru bond angle in the *Pbn2₁* phase is reduced by about 20° from that in the *Pbnm* phase. The pressure-induced phase transition is clearly against the structural rule in the literature for a perovskite and must be correlated to the peculiar electronic structure associated with low-spin Ru^{4+}: t_{2g}^4 and Pb^{2+}:$6s^2$ as they come closer under pressure.

We have measured the temperature dependence of resistance on crossing the *Pbnm* to *Pbn2₁* phase transition in $PbRuO_3$ under pressure in Fig. 2*C*. The $R(T)$ curve at $P = 0.53$ GPa obtained in a DAC reproduces essentially that measured on a grain of $PbRuO_3$ crystal in a piston-cylinder device (6). A sharp decrease in resistivity below 100 K with decreasing temperature is related to the phase transition to the *Imma* phase. This feature fades away gradually as pressure increases, which suggests that the low-temperature *Imma* phase is suppressed under pressure. Because of an improving electrical contact at grain boundaries and a broadening of the bandwidth, the resistance at room temperature (RRT) decreases under pressure. An increase of RRT on crossing the phase transition indicates that the *Pbn2₁* phase must have a narrower electronic bandwidth than that in the *Pbnm* phase at P_c. Despite the bandwidth narrowing, the *Pbn2₁* phase remains a bad metal. A huge residual resistance at $T = 0$ K and an extremely weak temperature dependence of the resistance make it like a large-polaron conductor.

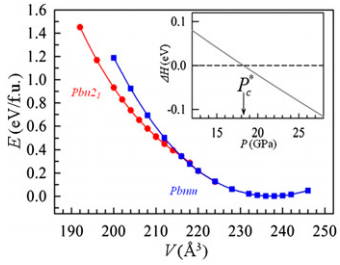

Fig. 3. Variations in the relative internal energies (*E*) per formula unit (f.u.) for the *Pbnm* and *Pbn2₁* phases of $PbRuO_3$ as a function of volume (*V*) from the LDA calculation. *Inset* shows the enthalpy difference between the *Pbnm* and *Pbn2₁* phases ($\Delta H = H_{Pbn21} - H_{Pbnm}$) as a function of pressure (*P*).

From a thermodynamic point of view, the relative stability between two different phases can be evaluated by their Gibbs free energy difference ($\Delta G = \Delta E + P\Delta V - T\Delta S$). The entropy contribution ($T\Delta S$) is typically on the order of magnitude of the thermal energy, which is much smaller than the internal energy change (ΔE). Hence, we only considered the enthalpy change ($\Delta H = \Delta E + P\Delta V$) at $T = 0$ K for simplicity. Fig. 3 shows calculated internal energy variations with respect to volume for the *Pbnm* and $Pbn2_1$ structures. By fitting the *E*–*V* data to the third-order BM equation, we obtained the ΔH versus *P* diagram (as shown in Fig. 3, *Inset*), which clearly demonstrates the crossover in *H* that favors the $Pbn2_1$ phase. The critical pressure is predicted to be $P_c^* = 18$ GPa in local-density approximation (LDA) and 27 GPa in generalized gradient approximations (GGA). Although the LDA has a well-known tendency to underestimate the phase-transition pressure (22), the GGA value is in good agreement with the experimental value of $P_c = 32$ GPa. In addition, both LDA and GGA calculations capture well other important aspects of the experimentally observed structural changes, including the evolution of lattice parameters, an abrupt volume drop on crossing P_c^*, and an anomalously short Pb—Ru bond in the *Pbn2₁* phase (see Fig. S4 and Tables S3 and S4 for the detailed information). We have also calculated enthalpy barriers for the *Pbnm* to *Pbn2₁* phase transformation by using the climbing image nudged elastic band method (23, 24). The predicted barrier decreases with increasing pressure; it reaches as small as 62 (48) meV at P_c^* with GGA (LDA), and it decreases with pressure. The relatively low energy barrier suggests that a facile phase transformation can take place even at room temperature.

Fig. 4 shows the electron density of states (DOS) projected on the atomic orbitals of the Pb, Ru, and O atoms in the *Pbnm* and *Pbn2₁* phases of $PbRuO_3$ from our LDA calculations; the corresponding band structures for the *Pbnm* and *Pbn2₁* structures at P_c^* are also presented. At ambient pressure, the DOS plot of Fig. 4*A* for the *Pbnm* phase shows overlap of the Pb 6*s*, Ru 4*d*, and O 2*p* orbitals in the energy range of $E_f - 3$ eV $< E < E_f + 1$ eV, which are largely attributed to the antibonding interactions of the Pb 6*s* and Ru t_{2g} orbitals with the O 2*p* orbitals. Notice also a minor contribution of the Pb 6*p* state overlapping with the Pb 6*s* state near the Fermi level, E_f. Our LDA calculation predicts the magnetic moment of the *Pbnm* phase to be negligible (0.2 μ_B per formula unit), consistent with experiments and other LDA calculations (5). The suppressed magnetic moment has been attributed to the Pb 6*s*–Ru t_{2g} and Pb 6*p*–Ru e_g hybridizations (aided by the O 2*p* state) as well as Ru t_{2g}–e_g mixing (5). The magnetic moment tends to be overestimated in GGA calculations, which is largely related to the well-known underbinding tendency of the GGA that results in the increase of lattice parameters and thus the reduced mixing of corresponding atomic orbitals.

As shown in Fig. 4*B*, increasing pressure to P_c^* leads to a broadening of the DOS peaks near the Fermi level in the *Pbnm* phase, apparently due to the increased overlap of the constituent atomic orbitals. The DOS analysis also shows some distinctly different features between the *Pbnm* and *Pbn2₁* phases. In the *Pbn2₁* case, Fig. 4*C*, the Pb 6*s* and 6*p* and Ru 4*d* peaks are noticeably enhanced in the energy range of $E_f - 2.6$ eV $< E < E_f -$ 1.4 eV. It turns out that this enhancement is attributable to a

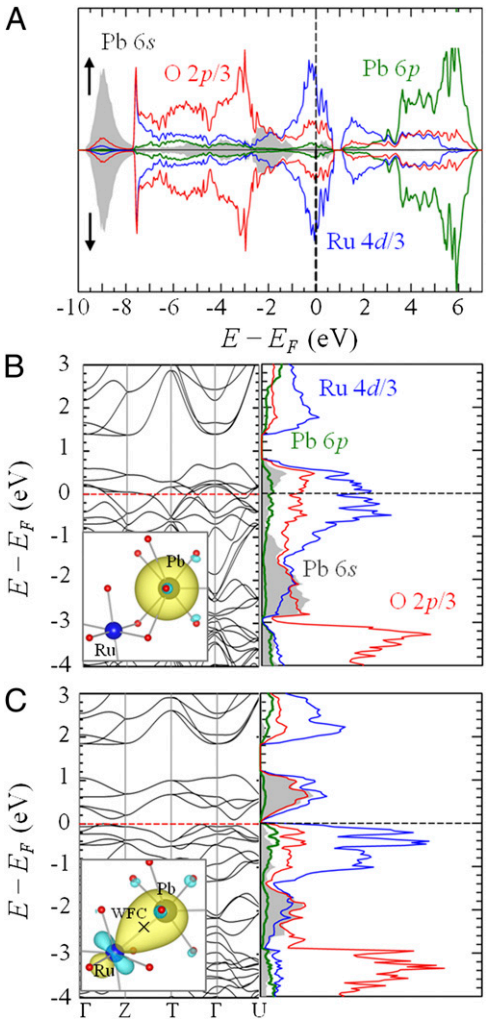

Fig. 4. (*A*) DOS projected on the Pb, Ru, and O atomic orbitals in the *Pbnm* phase of $PbRuO_3$ at $P = 0$ GPa; the arrows ↑ and ↓ indicate spin-up and spin-down, respectively. Band structures (*Left*) and DOS (*Right*) for the (*B*) *Pbnm* and (*C*) $Pbn2_1$ phases at high pressure ($P = 18$ GPa). Here, the Ru 4*d* and O 2*p* DOS are scaled by one-third, and the dotted lines indicated the Fermi level positions. The unbonded Pb 6*s* electron pair (*B*) and the bonding interaction between the Pb sp hybrid and Ru t_{2g} states (*C*) are also represented by maximally localized Wannier functions (with an isosurface value of 0.41 electron/Å^3) in the *Insets*, which were calculated using the Carr-Parrinello Molecular Dynamics (CPMP) package (29). In *C*, the WFC is indicated.

bonding interaction between the Pb *sp* hybrid and Ru t_{2g} orbitals, as demonstrated by crystal orbital overlap population (COOP) analysis (Fig. S5). The Pb—Ru bond formation is also well represented by the maximally localized Wannier function shown in Fig. 4*C*, *Inset*; note that the Wannier function center (WFC) (25) is located midway between the Pb and Ru atoms. Detailed charge density profiles for the *Pbnm* and $Pbn2_1$ structures are presented in Fig. S6. The covalent-like Pb—Ru bond formation appears to weaken the Ru 4*d*–O 2*p* interaction; the relatively reduced Ru 4*d*–O 2*p* overlap can be demonstrated by the band narrowing below the Fermi level (-1.4 eV $< E - E_f < 0$ eV) in comparison with the *Pbnm* case (Fig. 4*B*). The Pb—Ru bond formation leaves the corresponding antibonding orbitals completely empty and E_f is located at the leading edge of the bonding states, which accounts for the experimental observation that the $Pbn2_1$ phase remains a bad metal. We have also conducted the same calculation for isostructural $SrRuO_3$. The phase transition to the $Pbn2_1$ structure is not an option in $SrRuO_3$ under high pressure, which is consistent with experiment (26, 27).

In the polar $PbVO_3$ (28) the shortest distance between Pb and V in $PbVO_3$, d =3.35 Å, is still significantly longer than the d = 2.6 Å of the Pb—Ru bond length in the $Pbn2_1$ $PbRuO_3$. The following two observations make forming a chemical bond between Pb and Ru along the shortest distortion the primary driving force for the phase transition: (*i*) the presence of lone pair electrons leaves an anisotropic structure that has four equally short Pb—V distance whereas Pb is clearly bonded with one Ru ion in the $Pbn2_1$ $PbRuO_3$; (*ii*) from the plot of crystal orbital overlap population (COOP) in Fig. S5, the hybridization between the Pb:6*sp* and Ru4*d* is so strong that the COOP shows a clear bonding character on crossing the *Pbnm* to $Pnb2_1$ phase transition. We note that V^{4+} can form a strong double bond in the vanadyl $(V = O)^{2+}$ cation as a result of covalent bonding with $yz \pm izx$ orbitals, which allows the polar displacement of the vanadium in $PbVO_3$. In this case, the Pb:6*sp* lone pair also interacts with the $yz \pm izx$ π-bonding orbitals. The Ru^{4+} does not form a Ru = O cation, but its two holes occupy a narrow π* band in which there is no Hund stabilization of an intraatomic S = 1 state. Therefore, the two holes can occupy an a_1 orbital directed through the face of the octahedron to interact with a Pb:6*sp* lone pair. The strong Pb—Ru bond thus appears to be the driving force for the phase change.

In conclusion, $PbRuO_3$ undergoes a first-order transition from the orthorhombic *Pbnm* phase to a lower symmetry $Pbn2_1$ phase at $P_c = 32$ GPa. This observation violates the general trend of the perovskite oxides with $t \leq 1$ as a function of pressure. The $Pbn2_1$ phase has one very short Pb—Ru bond length. The RuO_6 octahedra are highly distorted to accommodate the unusually short Pb—Ru bond. The hybridization of the Pb sp and Ru t_{2g} orbitals, which increases dramatically in the *Pbnm* phase under pressure, is critical for the transition to the $Pbn2_1$ phase. Collapsing the Pb—Ru distance in the $Pbn2_1$ phase is associated with the formation of bonding and antibonding states from the strongly hybridized Pb sp and Ru t_{2g} orbitals.

Materials and Methods

The $PbRuO_3$ perovskite used in the present study has been prepared under 9 GPa and 1,400 °C with a Walk-type multianvil module (Rockland Research Co.). Details about the sample synthesis and characterizations can be found elsewhere (30). The in situ high-pressure angle-dispersive SXRD at room temperature was performed at the 16BM-D station of the Advanced Photon Source in the Argonne National Laboratory with a wavelength λ = 0.41326 Å by using a symmetric DAC of 300-μm culet diamonds. Neon gas and silicon oil have been used as the pressure-transmitting media. The ruby fluorescence method was used to monitor the pressure. The diffraction patterns were collected by using a MAR345 image-plate detector and then converted into the format of intensity versus 2θ by using FIT2D software. The structural information was extracted from Rietveld refinement of SXRD patterns with the FullProf program. The Raman spectroscopy measurements were conducted with a Renishaw in Via Spectrometer by using a symmetric Mao-Bell type DAC. The ruby fluorescence method was used to monitor the pressure. The measurements of ρ(T) up to 35 GPa were performed with a four-probe method in a DAC (31).

The calculations reported herein were performed on the basis of DFT within the LDA (32) and GGA-PBE (33) as implemented in the Vienna ab initio Simulation Package (VASP 5.2.2) (34). The projector-augmented wave method with a plane-wave basis set was used to describe the interaction between core and valence electrons (35). The valence-electron configurations considered are: $5d^{10}6s^26p^2$ for Pb; $4p^64d^75s^1$ for Ru; and $2s^22p^4$ for O. All $PbRuO_3$ structures were optimized with the conjugated gradient method until the residual forces on constituent atoms become smaller than 0.02 eV/Å. The cutoff energies for the plane-wave expansion were 700 and 500 eV for the geometry (cell shape and atomic position) optimization and electronic structure analysis, respectively. The Brillouin zone sampling was performed with a gamma-centered (6 × 6 × 4) Monkhorst–Pack *k*-point mesh (36) in the geometry optimization, and the *k*-point mesh size was increased up to (12 × 12 × 8) to reevaluate the corresponding electronic structures.

ACKNOWLEDGMENTS. This work was supported by the National Science Foundation (DMR-1122603) and the Welch Foundation (F-1066 and F-1535) and National Science Foundation of China and Ministry of Science and Technology in China. J.-F.L. and J.W. are supported by Energy Frontier Research in Extreme Environments (EFree) and the Carnegie/DOE Alliance Center (CDAC). High Pressure Synergetic Consortium at the Advanced Photon Source and High Pressure Collaborative Access Team were supported by Carnegie Institution of Washington, CDAC, University of Nevada, Las Vegas, and Lawrence Livermore National Laboratory through funding from Department of Energy (DOE)-National Nuclear Security Administration, DOE-Basic Energy Sciences and as a part of EFree, an Energy Frontier Research Center funded by the DOE under Award DE-SC0001057. The Texas Advanced Computing Center is also acknowledged for providing High Performance Computation resources.

1. Samara GA, Sakudo T, Yoshimitsu K (1975) Important generalization concerning the role of competing forces in displacive phase transitions. *Phys Rev Lett* 35(26):1767–1769.
2. Jabarov SG, et al. (2011) High-pressure effect on the ferroelectric-paraelectric transition in $PbTiO_3$. *Phys Solid State* 53(11):2300–2304.
3. Zhu J, et al. (2011) Thermal equations of state and phase relation of $PbTiO_3$: A high P-T synchrotron x-ray diffraction study. *J Appl Phys* 110(8):084103–084106.
4. Janolin PE, et al. (2008) High-pressure effect on $PbTiO_3$: An investigation by Raman and x-ray scattering up to 63 GPa. *Phys Rev Lett* 101(23):237601-1–23760-4.
5. Kimber SAJ, et al. (2009) Metal-insulator transition and orbital order in $PbRuO_3$. *Phys Rev Lett* 102(4):046409-1–046409-4.
6. Cheng JG, Zhou JS, Goodenough JB (2010) Evolution of ferromagnetism in orthorhombic perovskites $Sr_{1-x}Pb_xRuO_3$. *Phys Rev B* 81(13):134412-1–134412-6.
7. Glazer AM (1972) The classification of tilted octahedra in perovskites. *Acta Crystallogr B* 28(11):3384–3392.
8. Woodward PM (1997) Octahedral tilting in perovskites. I. Geometrical considerations. *Acta Crystallogr B* 53(1):32–43.
9. Woodward PM (1997) Octahedral tilting in perovskites. II. Structure stabilizing forces. *Acta Crystallogr B* 53(1):44–66.
10. Ali R, Yashima M (2005) Space group and crystal structure of the perovskite $CaTiO_3$ from 296 to 1720 K. *J Solid State Chem* 178(9):2867–2872.
11. Zhao Y (1998) Crystal chemistry and phase transitions of perovskite in P–T–X space: Data for $(K_xNa_{1-x})MgF_3$ perovskites. *J Solid State Chem* 141(1):121–132.
12. Ito E, Matsui Y (1978) Synthesis and crystal-chemical characterization of $MgSiO_3$ perovskite. *Earth Planet Sci Lett* 38(2):443–450.
13. Belik AA, Stefanovich SY, Lazoryak BI, Takayama-Muromachi E (2006) $BiInO_3$: A polar oxide with $GdFeO_3$-type perovskite structure. *Chem Mater* 18(7):1964–1968.
14. Yusa H, Belik AA, Takayama-Muromachi E, Hirao N, Ohishi Y (2009) High-pressure phase transitions in $BiMO_3$ (M=Al, Ga, and In): In situ x-ray diffraction and Raman scattering experiments. *Phys Rev B* 80(21):214103-1–214103-10.
15. O'Keeffe M, Hyde BG (1977) Some structures topologically related to cubic perovskite (E21), ReO_3 (D09) and Cu_3Au (L12). *Acta Crystallogr B* 33(12):3802–3813.
16. Zhou JS, Goodenough JB (2005) Universal octahedral-site distortion in orthorhombic perovskite oxides. *Phys Rev Lett* 94(6):065501-1–65501-4.
17. Kennedy BJ, Vogt T, Martin CD, Parise JB, Hriljac JA (2001) Pressure-induced orthorhombic to rhombohedral phase transition in $LaGaO_3$. *J Phys Condens Matter* 13(48): L925–L930.
18. Angel RJ, et al. (2007) High-pressure structural evolution of a perovskite solid solution $(La_{1-x}Nd_x)GaO_3$. *J Solid State Chem* 180(12):3408–3424.
19. Shibasaki T, et al. (2005) Exploration of high pressure phase in $LaGaO_3$ and $LaCrO_3$. *J Therm Anal Calorim* 81(3):575–581.
20. Zhou JS, Alonso JA, Muoñz A, Fernández-Díaz MT, Goodenough JB (2011) Magnetic structure of $LaCrO_3$ perovskite under high pressure from in situ neutron diffraction. *Phys Rev Lett* 106(5):057201.
21. Amboage M, Hanfland M, Alonso JA, Martínez-Lope MJ (2005) High pressure structural study of $SmNiO_3$. *J Phys Condens Matter* 17(11):S783–S788.
22. Zupan A, Blaha P, Schwarz K, Perdew JP (1998) Pressure-induced phase transitions in solid Si, SiO_2, and Fe: Performance of local-spin-density and generalized-gradient-approximation density functionals. *Phys Rev B* 58(17):11266–11272.
23. Sheppard D, Xiao P, Chemelewski W, Johnson DD, Henkelman G (2012) A generalized solid-state nudged elastic band method. *J Chem Phys* 136(7):074103–074108.
24. Henkelman G, Uberuaga BP, Jonsson H (2000) A climbing image nudged elastic band method for finding saddle points and minimum energy paths. *J Chem Phys* 113(22): 9901–9904.
25. Car R, Parrinello M (1985) Unified approach for molecular dynamics and density-functional theory. *Phys Rev Lett* 55(22):2471–2474.
26. Hamlin JJ, et al. (2007) AC susceptibility studies of the weak itinerant ferromagnet $SrRuO_3$ under high pressure to 34GPa. *Phys Rev B* 76(1):014432–014432-7.
27. Jacobsen MK, Kumar RS, Cao G, Neumeier JJ, Cornelius AL (2008) High pressure structural studies on $SrRuO_3$. *J Phys Chem Solids* 69(9):2237–2239.
28. Shpanchenko RV, et al. (2004) Synthesis, structure, and properties of new perovskite $PbVO_3$. *Chem Mater* 16(17):3267–3273.
29. Curioni A, Parrinello M, Wanda A (2013) Carr-Parrinello Molecular Dynamics. Available at www.cpmd.org. Accessed March 7, 2013.
30. Cheng JG, Zhou JS, Goodenough JB (2009) Metal-metal transition in perovskite $PbRuO_3$. *Phys Rev B* 80(17):174426–174426-5.
31. Zhang SJ, et al. (2009) Superconductivity at 31 K in the "111"-type iron arsenide superconductor $Na_{1-x}FeAs$ induced by pressure. *Eur Phys Lett* 88(4):47008.
32. Ceperley DM, Alder BJ (1980) Ground state of the electron gas by a stochastic method. *Phys Rev Lett* 45(7):566–569.
33. Perdew JP, Burke K, Ernzerhof M (1996) Generalized gradient approximation made simple. *Phys Rev Lett* 77(18):3865–3868.
34. Kresse G, Furthmüller J (2007) *Vienna Ab Initio Simulation Package: Users Guide* (The University of Vienna, Vienna, Austria).
35. Blöchl PE (1994) Projector augmented-wave method. *Phys Rev B* 50(24):17953–17979.
36. Monkhorst HJ, Pack JD (1976) Special points for Brillouin-zone integrations. *Phys Rev B* 13(12):5188–5192.